

GridDehazeNet+: An Enhanced Multi-Scale Network with Intra-Task Knowledge Transfer for Single Image Dehazing

Xiaohong Liu, *Graduate Student Member, IEEE*, Zhihao Shi, Zijun Wu, and Jun Chen, *Senior Member, IEEE*

Abstract—We propose an enhanced multi-scale network, dubbed GridDehazeNet+, for single image dehazing. It consists of three modules: pre-processing, backbone, and post-processing. The trainable pre-processing module can generate learned inputs with better diversity and more pertinent features as compared to those derived inputs produced by hand-selected pre-processing methods. The backbone module implements multi-scale estimation with two major enhancements: 1) a novel grid structure that effectively alleviates the bottleneck issue via dense connections across different scales; 2) a spatial-channel attention block that can facilitate adaptive fusion by consolidating dehazing-relevant features. The post-processing module helps to reduce the artifacts in the final output. To alleviate domain shift between network training and testing, we convert synthetic data to so-called translated data with the distribution shaped to match that of real data. Moreover, to further improve the dehazing performance in real-world scenarios, we propose a novel intra-task knowledge transfer mechanism that leverages the distilled knowledge from synthetic data to assist the learning process on translated data. Experimental results indicate that the proposed GridDehazeNet+ outperforms the state-of-the-art methods on several dehazing benchmarks. The proposed dehazing method does not rely on the atmosphere scattering model, and we provide a possible explanation as to why it is not necessarily beneficial to take advantage of the dimension reduction offered by this model, even if only the dehazing results on synthetic images are concerned.

Index Terms—Single image dehazing, attention-based feature fusion, intra-task knowledge transfer.

I. INTRODUCTION

THE image dehazing problem has received significant attention in the computer vision community over the past two decades. It aims to restore the clear version of a hazy image, thus helps mitigate the impact of image distortion induced by the environmental conditions on various visual analysis tasks.

The Atmosphere Scattering Model (ASM) [1]–[3] provides a simple approximation of the haze effect. Specifically, it assumes that

$$I_c(x) = J_c(x)t(x) + A(1 - t(x)), \quad c = 1, 2, 3, \quad (1)$$

where $I_c(x)$ ($J_c(x)$) is the intensity of the c th color channel of pixel x in the hazy (clear) image, $t(x)$ is the transmission map, and A is the global atmospheric light intensity. In addition, we have $t(x) = e^{-\beta d(x)}$, where β and $d(x)$ are

X. Liu, Z. Shi, Z. Wu, and J. Chen (Corresponding Author) are with the Department of Electrical and Computer Engineering, McMaster University, Hamilton, ON L8S 4K1, Canada (e-mail: {liux173, shiz31, wuz146, chen-jun}@mcmaster.ca). This work was supported in part by the Natural Sciences and Engineering Research Council of Canada through a Discovery Grant.

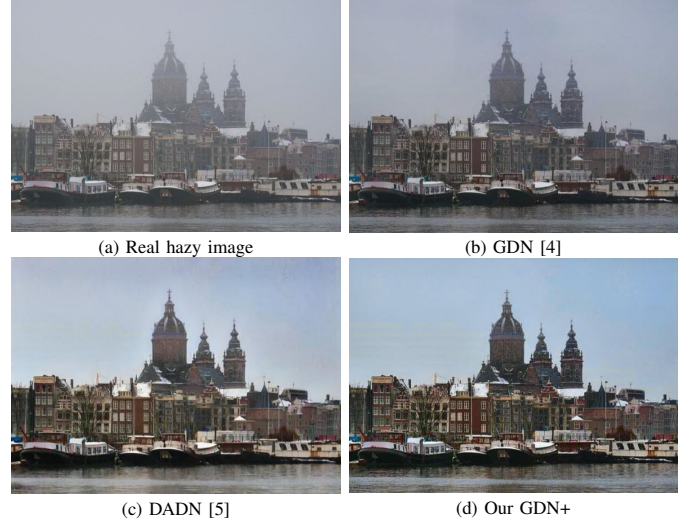


Fig. 1. Dehazing results for a real hazy image from the URHI dataset [6]: (a) the real hazy image, (b) the result based on GDN [4], (c) the result based on DADN [5], and (d) our result. Our GDN+ achieves the best visual performance against the others in terms of haze removal and color contrast.

the atmosphere scattering parameter and the scene depth, respectively. This model indicates that image dehazing is in general an underdetermined problem without the knowledge of A and $t(x)$.

As a canonical example of image restoration, the dehazing problem can be tackled using a variety of techniques that are generic in nature. Moreover, many misconceptions and difficulties encountered in image dehazing manifest in other restoration problems as well. Therefore, it is instructive to examine the relevant issues in a broader context, four of which are highlighted below.

1) *Role of Physical Model*: Many data-driven approaches to image restoration require synthetic data for training. To produce such data, it is necessary to have a physical model of the relevant image degradation process (e.g., the ASM for the haze effect). A natural question arises whether the design of the image restoration algorithm itself should rely on this physical model. Apparently a model-dependent algorithm may suffer inherent performance loss on real images due to model mismatch. However, it is often taken for granted that such an algorithm must have advantages on synthetic images produced using the same physical model.

2) *Selection of Pre-Processing Method*: Pre-processing is widely used in image preparation to facilitate follow-up opera-

tions [7], [8]. It can also be used to generate several variants of the given image, providing a certain form of diversity that can be harnessed via proper fusion. However, the pre-processing methods are often selected based on heuristics, thus are not necessarily best suited to the problem under consideration.

3) *Bottleneck of Multi-Scale Estimation*: Image restoration requires an explicit/implicit knowledge of the statistical relationship between the distorted image and the original clear version. The statistical model needed to capture this relationship often has a huge number of parameters, comparable or even more than the available training data. As such, directly estimating these parameters based on the training data is often unreliable. Multi-scale estimation [9], [10] tackles this problem by i) approximating the high-dimensional statistical model with a low-dimensional one, ii) estimating the parameters of the low-dimensional model based on the training data, iii) parameterizing the neighborhood of the estimated low-dimensional model, performing a refined estimation, and repeating this procedure if needed. It is clear that the estimation accuracy on one scale will affect that on the next scale. Since multi-scale estimation is commonly done in a successive manner, its performance is often limited by a certain bottleneck.

4) *Effect of Domain Shift*: The effectiveness of supervised learning for image restoration has been widely observed. However, building a large-scale real dataset of distorted images paired with their ground-truth is very expensive and sometimes not even possible [11]. Therefore, in practice one commonly resorts to synthetic data for network training. However, due to domain shift, there is no guarantee that a network trained on synthetic data can generalize well over to real data.

The present work can be viewed as a product of our attempt to address the aforementioned generic issues in image restoration. Its main contributions can be summarized as follows:

- 1) The proposed GridDehazeNet+ (GDN+) does not rely on the ASM for haze removal, yet is capable of outperforming the existing model-dependent dehazing methods even on synthetic images. A possible explanation, together with some supporting experimental results, is provided for this puzzling phenomenon.
- 2) In contrast to hand-selected pre-processing methods, the pre-processing module in the GDN+ is fully trainable, thus can offer more flexible and pertinent image enhancement.
- 3) The implementation of attention-based multi-scale estimation on a densely connected grid network allows efficient information exchange across different scales and alleviates the bottleneck issue.
- 4) To cope with domain shift and improve the dehazing performance on real hazy images, we introduce a novel Intra-Task Knowledge Transfer (ITKT) mechanism that leverages the distilled knowledge from synthetic data to assist the learning process on translated data.

Benefiting from the overall design, the proposed GDN+ outperforms the State-Of-The-Art (SOTA) methods on several dehazing benchmarks. An example is shown in Fig. 1, where our method delivers the most visually appealing dehazing result for a sample real hazing image from the URHI dataset [6].

II. RELATED WORK

Early works on image dehazing either require *multiple* images of the same scene taken under different conditions [2], [12]–[15] or side information acquired from other sources [16], [17]. Recent years have seen increasing interest in *single* image dehazing without side information, which is considerably more challenging. To place our work in a proper context, we give a brief review of the existing prior-based and learning-based methods for single image dehazing as well as the recent developments of knowledge distillation and transfer.

A. Prior-Based Single Image Dehazing

A conventional strategy for single image dehazing is to estimate the transmission map $t(x)$ and the global atmospheric light intensity A (or their variants) based on certain assumptions or priors then invert Eq. (1) to obtain the dehazed image. Representative works along this line of research include [18]–[22]. Specifically, reference [18] proposes a local contrast maximization method for dehazing, motivated by the observation that clear images tend to have higher contrast as compared to their hazy counterparts; in [19], haze removal is realized via the analysis of albedo under the assumption that the transmission map and surface shading are locally uncorrelated; the dehazing method introduced in [20] makes use of the Dark Channel Prior (DCP), which asserts that pixels in non-haze patches have low intensity in at least one color channel; reference [21] suggests a machine learning approach that exploits four haze-related features using a random forest regressor; the color attenuation prior is adopted in [22] for the development of a supervised learning method for image dehazing. Although these methods have enjoyed varying degrees of success, their performances are inherently limited by the accuracy of the adopted assumptions/priors with respect to the target scenes.

B. Learning-Based Single Image Dehazing

With the advance in deep learning techniques and the availability of large synthetic datasets [21], recent years have witnessed the increasing popularity of data-driven methods for image dehazing. These methods largely follow the conventional strategy mentioned above but with reduced reliance on hand-crafted priors. For example, reference [23] employs a multi-scale CNN that is able to perform refined transmission estimation; the dehazing method, DehazeNet, proposed in [24] uses a three-layer Convolutional Neural Network (CNN) to directly estimate the transmission map from the given hazy image; in [25], the ASM is embedded into a neural network for joint learning of the transmission map, atmospheric light intensity and dehazed image; reference [26] explores the physical model in the feature space (instead of the pixel space) to perform image dehazing.

The AOD-Net [27] represents a departure from the conventional strategy. Specifically, a reformulation of Eq. (1) is introduced in [27] to bypass the estimation of the transmission map and atmospheric light intensity. A close inspection reveals that this reformulation in fact renders the ASM completely

superfluous (though this point is not recognized in [27]). The Gated Fusion Network (GFN) proposed in [8] goes one step further by explicitly abandoning the ASM in its design, and leverages several hand-selected pre-processing methods (namely, white balance, contrast enhancing, and gamma correction) to improve the dehazing results. By regarding the image dehazing problem as an image-to-image translation problem, reference [28] proposes an Enhanced Pix2pix Dehazing Network (EPDN) based on the Generative Adversarial Network (GAN), which does not rely on the physical model.

While there is increasing evidence that model-agnostic image dehazing methods are able to outperform their model-dependent counterparts even if only synthetic data (produced using the physical model) are concerned, the reason behind this puzzling phenomenon is still unclear. In this paper, we attempt to lift the veil by providing a possible explanation together with some supporting experiments.

Learning-based methods trained using synthetic data tend to generalize poorly over to real data due to domain shift. To mitigate the detrimental effect caused by domain shift, reference [29] proposes a hybrid approach, where a CNN is trained on synthetic data in a supervised manner and on real data in an unsupervised manner. However, involving real data in training does not fully address the domain-shift issue. In its subsequent work [5], a Domain Adaptation Dehazing Network (DADN) is proposed, where the CycleGAN [11] is employed for adaptation between the synthetic domain and real domain. The present paper further develops and simplifies this idea by showing how to make effective use of so-called translated data to reduce the domain discrepancy.

C. Knowledge Distillation and Transfer

One popular application of knowledge distillation [30] is for network compression, where the learned logits from a large network (*i.e.*, teacher) is transferred to a small network (*i.e.*, student) that is much easier for deployment, possibly at the cost of a performance drop. Reference [31] suggests that the intermediate representations from the teacher can be leveraged to further improve the training process of the student. In recent years, knowledge distillation has been proved useful not only for network compression, but also for various computer vision tasks, including object detection [32], semantic segmentation [33], image synthesis [34], style transfer [35], *etc.* To the best of our knowledge, knowledge distillation finds its first application to single image dehazing in [36], where the teacher and student share the same architecture but are responsible for image reconstruction and image dehazing, respectively. In contrast, reference [37] proposes a Knowledge Distilling Dehazing Network (KDDN), where the architectures of teacher and student are tailored to their respective tasks. Moreover, multiple features, instead of using only one intermediate feature [36], are distilled in [37] to achieve better dehazing performance.

Different from [36], [37] where knowledge transfer is carried out among heterogeneous tasks, we perform ITKT with the teacher and student *both* working on the dehazing task but taking synthetic data and translated data as their respective

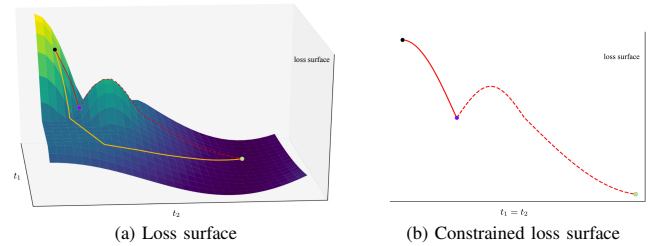


Fig. 2. On the potential detrimental effect of using the ASM for image dehazing. For illustration purposes, we focus on two color channels of a single pixel and denote the respective transmission maps by t_1 and t_2 . Fig. 2 (a) plots the loss surface as a function of t_1 and t_2 . It can be seen that the global minimum is attained at a point (see the green dot) satisfying $t_1 = t_2$, which agrees with the ASM. With the black dot as the starting point, one can readily find this global minimum using gradient descent (see the yellow path). However, a restricted search based on the ASM along the $t_1 = t_2$ direction (see the red path) will get stuck at a point indicated by the purple dot (see Fig. 2 (b)). Note that this point is a local minimum in the constrained space but not in the original space, and it becomes an obstruction simply due to the adoption of the ASM.

inputs. Intuitively, dealing with synthetic data generated by the ASM yields useful insights into translated data from the real domain, where the haze effect does not admit a simple mathematical characterization. Therefore, the characteristics of intermediate features distilled from the teacher network trained on synthetic data can greatly help the learning process of the student network on translated data, enabling it to deliver satisfactory dehazing results in real-world scenarios.

III. METHOD

A. Overview

Here we highlight the following aspects of the proposed GDN+.

1) No Reliance on the Atmosphere Scattering Model:

Although the model-agnostic approach to single image dehazing has become increasingly popular, no convincing reason has been provided why there is any advantage in ignoring the ASM, as far as the dehazing performance on synthetic images is concerned. The argument put forward in [8] is that estimating $t(x)$ from a hazy image is an ill-posed problem. Nevertheless, this is puzzling since estimating $t(x)$ (which is color-channel-independent) is presumably easier than $J_c(x)$, $c = 1, 2, 3$. In Fig. 2, we offer a possible explanation why it could be problematic if one blindly uses the fact that $t(x)$ is color-channel-independent to narrow down the search space and why it might be potentially advantageous to relax this constraint in the search of the optimal $t(x)$. However, with this relaxation, the ASM offers no dimension reduction in the estimation procedure. More fundamentally, it is known that the loss surface of a CNN is generally well-behaved in the sense that the local minima are often almost as good as the global minimum [38]–[40]. On the other hand, by incorporating the ASM into a CNN, one basically introduces a nonlinear component that is heterogeneous in nature from the rest of the network, which may create an undesirable loss surface. To support this explanation, we provide some experimental results in Section V-D.

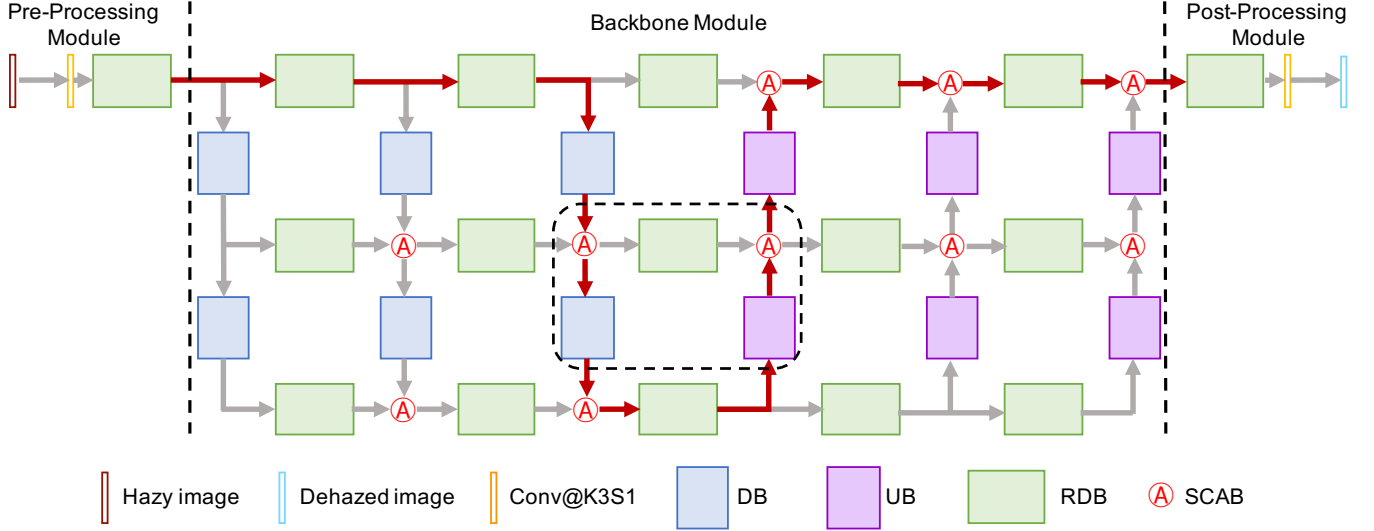


Fig. 3. The architecture of the proposed GridDehazeNet+ (GDN+). Here Conv@K n S m indicates a $n \times n$ convolution with stride m .

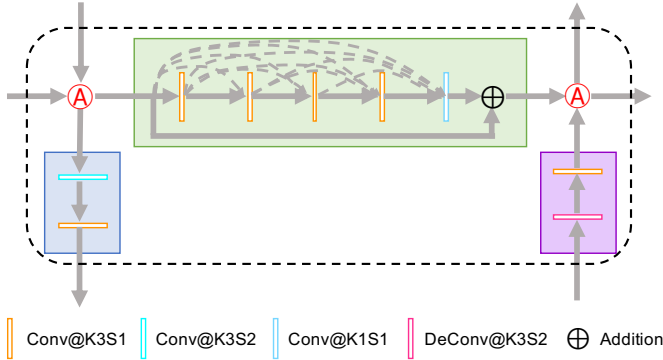


Fig. 4. Illustration of the dashed box in Fig. 3. Here Conv(DeConv)@K n S m indicates a $n \times n$ convolution (deconvolution) with stride m .

2) *Trainable Pre-Processing Module*: The pre-processing module effectively converts the single image dehazing problem to a multi-image dehazing problem by generating several variants of the given hazy image, each highlighting a different aspect of this image and making the relevant feature information more evidently exposed. In contrast to those hand-selected pre-processing methods adopted in the existing works (e.g., [8]), the proposed pre-processing module is made fully trainable, which is in line with the general preference of data-driven methods over prior-based methods as shown by recent developments in image dehazing. Note that hand-selected processing methods typically aim to enhance certain concrete features that are visually recognizable. However, the exclusion of abstract features is not justifiable. Indeed, there might exist abstract transform domains that better suit the follow-up operations than the image domain. A trainable pre-processing module has the freedom to identify transform domains over which more diversity gain can be harnessed.

3) *Enhanced Multi-Scale Estimation*: Here the meaning of the word *enhanced* is two-fold. First, inspired by [41], we *enhance* the conventional multi-scale network using a novel

grid structure. This grid structure has clear advantages over the encoder-decoder structure and the conventional multi-scale structure extensively used in image restoration [8], [42]–[44]. In particular, the information flow in the encoder-decoder structure or the conventional multi-scale structure often suffers from the bottleneck effect due to the hierarchical architecture whereas the grid structure circumvents this issue via dense connections across different scales using up-sampling/down-sampling blocks. Second, we further *enhance* the network with Spatial-Channel Attention Blocks (SCABs) that are placed at the junctions where features are exchanged and aggregated. These SCABs enable the network to better exploit the diversity created by the pre-processing module and the information most relevant to the dehazing task.

4) *Intra-Task Knowledge Transfer*: ITKT refers to leveraging the knowledge acquired from a certain task on one dataset to facilitate the learning process of the same task on another dataset. In the current context, it is observed that the knowledge distilled from ASM-based synthetic data is beneficial for handling translated data. As such, to further improve the dehazing performance on real hazy images, rather than directly performing training on translated data, a teacher-student structure is adopted: the GDN+ is used for both teacher and student; the teacher network is first trained on synthetic data and the acquired knowledge is transferred to the student network that is trained on the translated data. To the best of our knowledge, this is the first work that leverages ITKT to improve the dehazing performance in real-world scenarios.

Compared with its preliminary version GDN reported in [4], the GDN+ is refined in two aspects. The GDN only adopts channel-wise attention with the learned weights independent to the target features [4]. In contrast, the GDN+ employs the self-attention mechanism [45], [46], encapsulated in SCABs, to generate feature-adaptive weights. In addition, the GDN+ is designed with domain shift in mind. It is observed that the GDN tends to suffer significant performance degradation in real-world scenarios, possibly due to the domain discrepancy

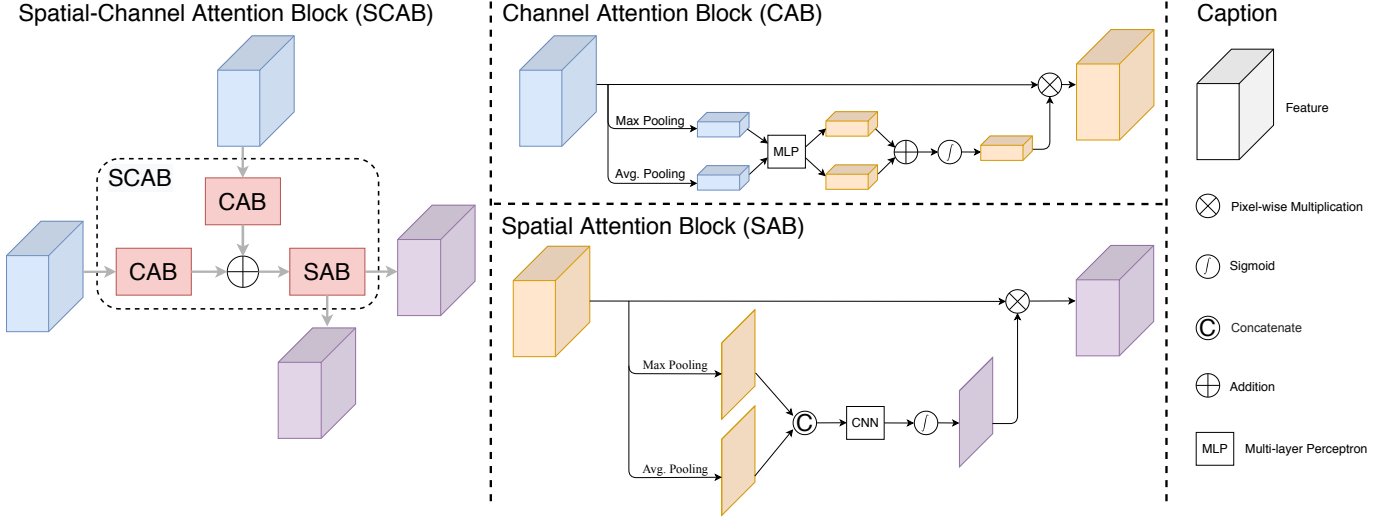


Fig. 5. Illustration of the Spatial-Channel Attention Block (SCAB).

between synthetic hazy images used for training and real hazy images used for testing. To address this issue, inspired by [5], we convert synthetic data to translated data with the distribution matched to that of real data, and leverage the latter for training. Moreover, we regard the knowledge gained from synthetic data as a prior to facilitate the learning process on translated data, and use a teacher-student structure to realize knowledge transfer.

B. Network Architecture

The GDN+ consists of three modules, namely, the pre-processing module, the backbone module and the post-processing module. Fig. 3 shows the overall architecture of the proposed network.

The pre-processing module consists of a 3×3 convolution with stride 1 (denoted as Conv@K3S1) and a Residual Dense Block (RDB) [43]. It generates 16 feature maps, which will be referred to as the learned inputs, from the given hazy image.

The backbone module is an improved version of Grid-Net [41] originally proposed for semantic segmentation. It performs enhanced multi-scale estimation based on the learned inputs. We choose a grid structure with three rows and six columns. Each row corresponds to a different scale and consists of five RDBs with the number of feature maps unaltered. Each column can be regarded as a bridge that connects different scales via Upsampling Blocks (UBs) or Downsampling Blocks (DBs). In each UB (DB), the size of feature maps is increased (decreased) by a factor of 2 while the number of feature maps is decreased (increased) by the same factor. Here upsampling/downsampling is implemented using convolution instead of traditional methods such as bilinear or bicubic interpolation. Fig. 4 provides a detailed illustration of the RDB, UB and DB in the dash box in Fig. 3. Each RDB consists of five convolutions: the first four are used to increase the number of feature maps while the last one fuses these feature maps. The output is then combined with the input of this RDB via channel-wise addition. Following [43],

the growth rate in RDB is set to 16. The UB and DB are structurally the same except that they respectively use Convolution (Conv) and DeConvolution (DeConv)) to adjust the size of feature maps. In the proposed GDN+, except for the first convolution in the pre-processing module and the 1×1 convolution in each RDB, all other convolutions are activated by ReLU. To strike a balance between the output size and the computational complexity, we set the number of feature maps at three different scales to 16, 32, and 64, respectively.

The dehazed image constructed directly from the output of the backbone module tends to contain artifacts. As such, we introduce a post-processing module to improve the quality of the dehazed image. The structure of the post-processing module is symmetrical to that of the pre-processing module.

It is worth noting that the GDN+ subsumes some existing networks as special cases. For example, the red path in Fig. 3 shows an encoder-decoder network that can be obtained by pruning the GDN+. As another example, removing the exchange branches (*i.e.*, the middle four columns in the backbone module) from the GDN+ leads to a conventional multi-scale network.

C. Feature Fusion with Spatial-Channel Attention Blocks

Since different channels and regions of learned features may not be of the same importance for the dehazing process, we embed certain judiciously constructed SCABs into the network to enable adaptive feature fusion. The SCAB employs spatial and channel-wise attentions [46], realized respectively by the Spatial Attention Block (SAB) and the Channel Attention Block (CAB). The SAB applies the average and max poolings along the channel axes to aggregate the local information on different feature maps, and the two pooled results are concatenated and fed into a convolution to generate the spatial attention map. The CAB applies the average and max poolings along the spatial axes instead; the pooled features are adjusted by a shared multi-layer perceptron which explores the inter-channel relationship to consolidate the important information;

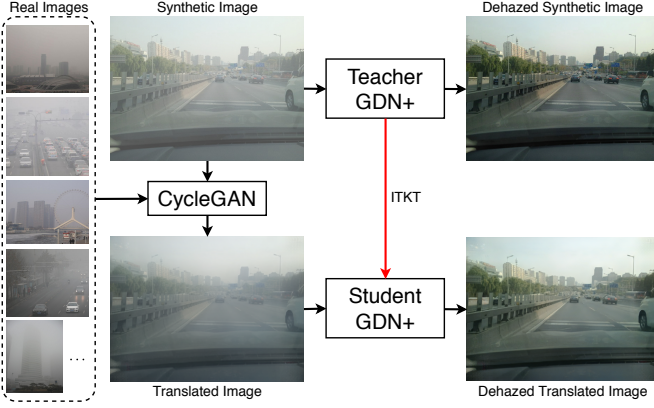


Fig. 6. The flowchart of the proposed Intra-Task Knowledge Transfer (ITKT) mechanism.

the adjusted versions are then added together and passed through a Sigmoid function to produce the channel attention coefficients. Finally, the spatial attention map and channel attention coefficients act back on the corresponding input features to enable self-adaptation.

As illustrated in Fig. 5, each SCAB consists of two CABs and one SAB. The features from horizontal and vertical streams are first accommodated by two distinct CABs to strengthen the relevant characteristics via channel-wise attention. The outputs of the two CABs are added together and then fed into a SAB for spatial adaptation. Let $F_{i,j}^h$ and $F_{i,j}^v$ denote respectively the features from the horizontal stream and vertical stream at the fusion position (i, j) in the backbone module, where $i = 0, 1, 2$ and $j = 0, 1, \dots, 5$. Let $f_{i,j}^h(F | \Theta_{i,j}^h)$ and $f_{i,j}^v(F | \Theta_{i,j}^v)$ denote respectively the CAB operations for the horizontal stream and vertical stream at the fusion position (i, j) , where F represents an arbitrary input feature, and $\Theta_{i,j}^h, \Theta_{i,j}^v$ are the trainable weights. Similarly, let $g_{i,j}(F | \Phi_{i,j})$ denote the SAB operation at the fusion position (i, j) , where $\Phi_{i,j}$ is the trainable weight. The proposed SCAB can be expressed as

$$\tilde{F}_{i,j} = g_{i,j}(f_{i,j}^c(F_{i,j}^c | \Theta_{i,j}^c) + f_{i,j}^r(F_{i,j}^r | \Theta_{i,j}^r) | \Phi_{i,j}), \quad (2)$$

where $\tilde{F}_{i,j}$ is the output feature of the SCAB. Note that SCABs endow the GDN+ with the ability to fuse features from different scales adaptively. Quite remarkably, our experimental results indicate that it suffices to use SCABs with a small number of trainable weights to substantially boost the overall performance.

D. Intra-Task Knowledge Transfer

To alleviate domain shift between network training and testing, we use the CycleGAN [11] to convert ASM-based synthetic data to more realistic-looking translated data. As the real haze effect captured by translated data does not admit a simple mathematical characterization, the learning process on translated data is more difficult than that on synthetic data. Inspired by the easy-to-difficult learning behavior of human beings, we propose an ITKT mechanism based on a teacher-student structure. The teacher network is first trained on

synthetic data to distill knowledge from this relatively simple task. Then the distilled knowledge is regarded as a *prior* to assist the more challenging learning process of the student network on translated data. Moreover, for the sake of feature alignment, our teacher and student networks adopt the same architecture (*i.e.*, GDN+).

The overall flowchart of the proposed ITKT mechanism is demonstrated in Fig. 6. It can be seen that the haze effect exhibited by the synthetic image is noticeably different from that by the translated image, which is a clear indicator of domain shift. Benefiting from the introduction of ITKT, the dehazing performance on real hazy images is greatly improved. In Sec. V-G, we also evaluate the effectiveness of ITKT by removing the teacher network and directly training the student network on translated data. Our experimental results show that the dehazing performance deteriorates as a consequence of this change.

E. Loss Function

In total, three different loss functions are employed to train the proposed network: 1) the fidelity loss L_F , 2) the perceptual loss L_P , and 3) the intra-task knowledge transfer loss L_{KT} . Their definitions and the underlying rationale are detailed below.

1) *Fidelity Loss*: The commonly used fidelity losses include L_1 and MSE. The MSE loss is very sensitive to outliers, thus might suffer from gradient explosion [47]. Although the L_1 loss does not have this issue, it is not differentiable at zero. The smooth L_1 loss can be regarded as an integration of these two losses, thus inherits their merits and avoids their drawbacks. Therefore, we use it as our fidelity loss to quantitatively measure the difference between the dehazed image and the ground-truth.

Let $\hat{J}_c(x)$ denote the intensity of the c th color channel of the pixel x in the dehazed image, and N denote the total number of pixels in one channel. Our fidelity loss can be expressed as

$$L_F = \frac{1}{3N} \sum_{c=1}^3 \sum_{x=1}^N h(\hat{J}_c(x) - J_c(x)), \quad (3)$$

where

$$h(e) = \begin{cases} 0.5e^2, & \text{if } |e| < 1, \\ |e| - 0.5, & \text{otherwise.} \end{cases} \quad (4)$$

2) *Perceptual Loss*: As a complement to the pixel-level fidelity loss, the perceptual loss [48] leverages multi-scale features extracted from a pre-trained deep neural network to quantify the overall *perceptual* difference between the dehazed image and the ground-truth. In this work, we use the VGG16 [49] pre-trained on ImageNet [50] as our loss network and extract the features from the last layer of each of the first three stages (*i.e.*, Conv1-2, Conv2-2 and Conv3-3). The perceptual loss can be defined as

$$L_P = \frac{1}{3} \sum_{l=1}^3 \frac{1}{C_l H_l W_l} \|\phi_l(\hat{J}) - \phi_l(J)\|_2^2, \quad (5)$$

where $\phi_l(\hat{J})$ ($\phi_l(J)$), $l = 1, 2, 3$, denote the aforementioned three VGG16 feature maps associated with the dehazed image

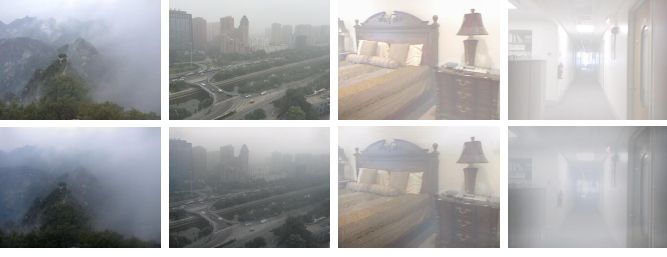


Fig. 7. Visualization of the haze effect before (shown in the 1st row) and after (shown in the 2nd row) the translation.

\hat{J} (the ground truth J), and C_l , H_l , and W_l specify the dimension of $\phi_l(\hat{J})$ ($\phi_l(J)$).

3) *Intra-Task Knowledge Transfer Loss*: For the features from the teacher network to serve as a prior to facilitate the learning process of the student network, we design an ITKT loss that guides the features from the student network to mimic the ones from the teacher network by reducing their L_1 distance. Three intermediate features from the first scale of the backbone module after the SCAB-based fusion are selected to be involved in knowledge transfer. According to our experiments, this selection induces the best dehazing performance among the candidates that have been considered. Following the notation in Sec. III-C, we denote these features by $\tilde{F}_{0,3}$, $\tilde{F}_{0,4}$, $\tilde{F}_{0,5}$, and use the superscripts t and s to indicate whether they come from the teacher or student network. Our ITKT loss can be expressed as

$$L_{KT} = \frac{1}{3} \sum_{j=3}^5 \|\tilde{F}_{0,j}^s - \tilde{F}_{0,j}^t\|_1. \quad (6)$$

4) The Overall Losses for Teacher and Student Networks:

The overall loss for the teacher network (denoted as L_T) is a linear combination of fidelity and perceptual losses. It can be formulated as

$$L_T = L_F + \lambda_P L_P, \quad (7)$$

where λ_P is used to balance the two loss components, and is set to 0.04. As for the student network, its loss function (denoted as L_S) integrates fidelity and perceptual losses as well as the ITKT loss. Specifically, we have

$$L_S = L_F + \lambda_P L_P + \lambda_{KL} L_{KL}, \quad (8)$$

where λ_{KL} plays a similar role as λ_P , and is set to 0.01.

IV. DATA PREPARATION

A. Training Dataset

Our teacher and student networks are trained using different datasets. For the teacher network, we adopt a large-scale synthetic dataset, named RESIDE [6]. This dataset contains synthetic hazy images of indoor and outdoor scenes, generated from clear images based on the ASM via proper choice of the scattering coefficient β and the atmospheric light intensity A . The Indoor Training Set (ITS) of RESIDE has a total of 13,990 hazy images, generated from 1,399 clear images with $\beta \in [0.6, 1.8]$ and $A \in [0.7, 1.0]$ (the depth maps $d(x)$ are obtained from the NYU Depth V2 dataset [51]

and Middlebury Stereo dataset [52]). We observe that there is an overlap between the Outdoor Training Set (OTS) and the Synthetic Objective Testing Set (SOTS) of RESIDE in the sense that some clear images are used to generate hazy versions in both sets (though the adopted ASM parameters are different). With the overlapped part removed, the OTS has a total of 296,695 hazy images, generated from 8,477 clear images with $\beta \in [0.04, 0.2]$ and $A \in [0.8, 1.0]$ (the depth maps are estimated using the algorithm in [53]). To build the training dataset for the student network, we select 3,000 synthetic images respectively from ITS and OTS as well as 1,000 real images from the Unannotated Real Hazy Images (URHI) dataset [6]. The CycleGAN is used to convert these 6,000 synthetic images to translated images with the distribution matched to that of the selected 1,000 real images. Then we leverage the resulting translated data to train the student network. Fig. 7 visualizes the haze effect before and after this translation.

B. Testing Dataset

For testing, in total 6 dehazing benchmarks are used. Four of them are synthetic datasets and the rest two are real datasets. The four synthetic datasets are 1) SOTS, 2) Middlebury [54], 3) HazeRD [55], and 4) O-HAZE [56]. The haze effect in the first three datasets is simulated by the ASM. In contrast, for O-HAZE, the haze effect is produced by a professional haze machine. We follow the same training/testing splits as in [57] to finetune our model and the compared methods to ensure fairness. The two adopted real datasets are 1) 37Real [58] and 2) URHI [6]. The teacher GDN+ is tested on the synthetic datasets to demonstrate the superiority of the network design while the student GDN+ is tested on the real datasets to verify the effectiveness of the proposed ITKT mechanism.

V. EXPERIMENTAL RESULTS

We conduct extensive experiments to demonstrate that the proposed GDN+ outperforms the SOTA dehazing methods on both synthetic and real datasets. The experimental results also provide useful insights into the constituent modules of the GDN+ and solid justifications for the overall design. We end this section with the runtime analysis and the discussion of a potential failure case.

A. Experimental Setup

We train the teacher and student networks on synthetic and translated data separately. Since there are more than 310k synthetic images with ITS and OTS combined, it is inefficient to train the teacher network on such a massive dataset. Therefore, we uniformly sample 6,000 images from ITS and OTS respectively to gather a total number of 12,000 images for one training epoch. To train the student network, we use the aforementioned 6,000 translated hazy images. Besides, the corresponding synthetic images are fed into the teacher network to produce the features needed for ITKT. We perform training using RGB images patches of size 240×240 . The Adam optimizer [59] is adopted, where β_1 and β_2 take the

TABLE I
QUANTITATIVE EVALUATIONS ON FOUR DEHAZING BENCHMARKS. AVERAGE PSNR/SSIM VALUES ARE REPORTED. **RED** AND **BLUE** INDICATE THE BEST AND THE SECOND BEST PERFORMANCE, RESPECTIVELY.

Method	DCP	DehazeNet	AOD-Net	GFN	EPDN	DADN	KDDN	GDN	GDN+
SOTS	15.49/0.64	21.14/0.85	19.06/0.85	22.30/0.88	23.82/0.89	27.76/0.93	30.09/ 0.97	31.51/0.98	32.15/0.98
Middlebury	15.91/0.81	13.28/0.79	13.86/0.79	14.38/0.81	15.11/0.83	15.93/0.70	17.27/0.87	16.70/0.85	18.04/0.88
HazeRD	14.01/0.39	15.54/0.41	15.63/0.45	13.98/0.37	17.37/0.56	18.07/0.63	16.44/ 0.83	16.06/ 0.83	19.54/0.87
O-HAZE	15.80/0.33	19.37/0.64	18.85/0.70	22.83/0.77	19.82/0.75	21.69/0.74	25.46/0.78	23.51/ 0.83	26.10/0.85

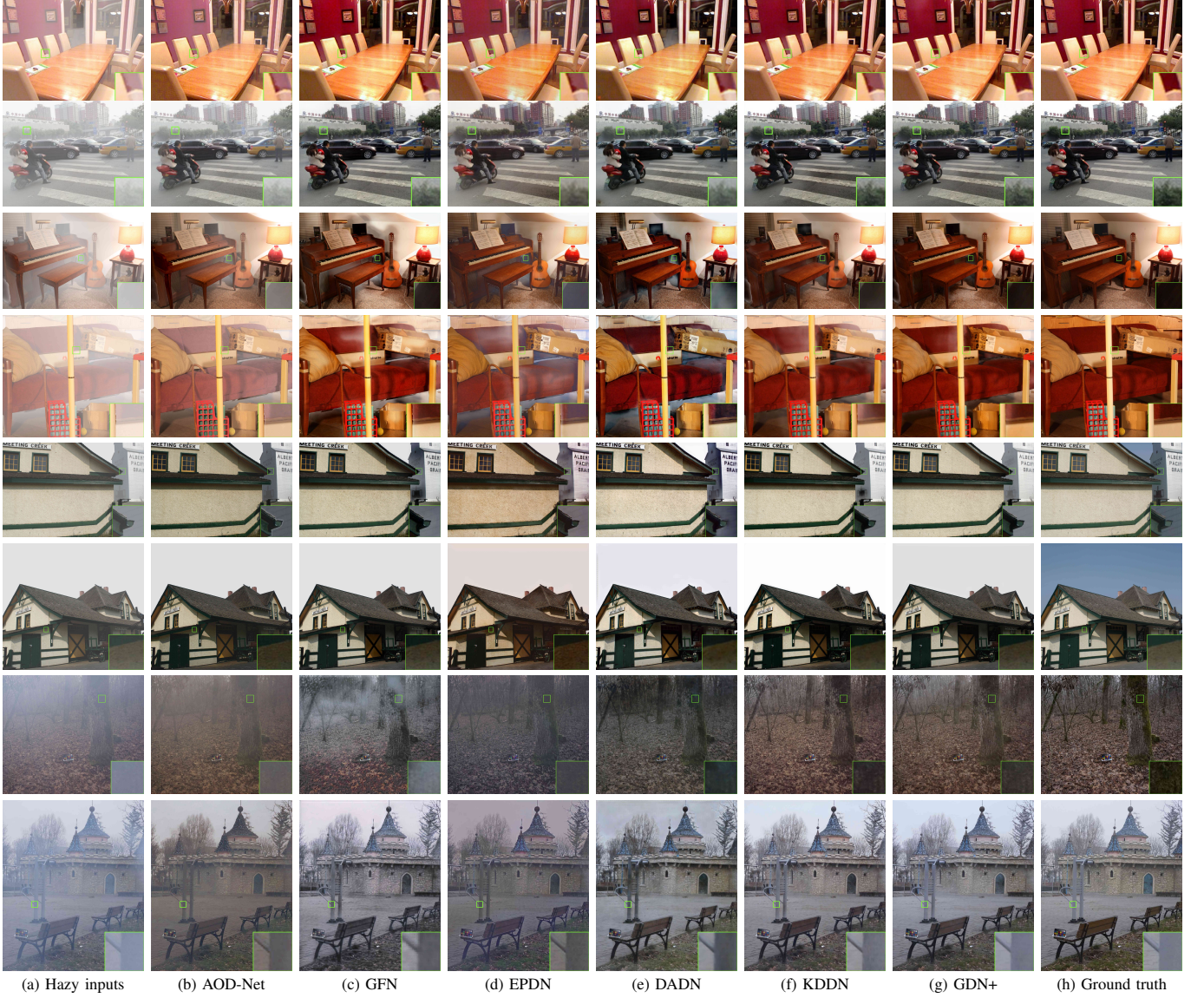


Fig. 8. Visual comparisons of different methods on synthetic datasets: SOTS, Middlebury, HazeRD, and O-HAZE (from top to bottom with two rows for each dataset). Zoom in for details.

default values of 0.9 and 0.999, respectively. The batch size is set to 16 with the initial learning rate $1e-3$. Following [60], [61], we do not use batch normalization. We train each network for 100 epochs, and the learning rate is reduced by half every 20 epochs. The training is carried out on a PC with two NVIDIA GeForce GTX 2080Ti, but only one GPU is used for testing.

We compare the proposed GDN+ with 8 methods includ-

ing DCP [20], DehazeNet [24], AOD-Net [27], GFN [8], EPDN [28], DADN [5], KDDN [37], and GDN [4], where the DCP is a prior-based method and the others are all learning-based methods. Since the KDDN reports the SOTA performance on synthetic test dataset and the DADN achieves the SOTA results in real-world scenarios, they are considered as the representatives of the existing dehazing methods. For quantitative comparisons, we leverage the Peak Signal to Noise

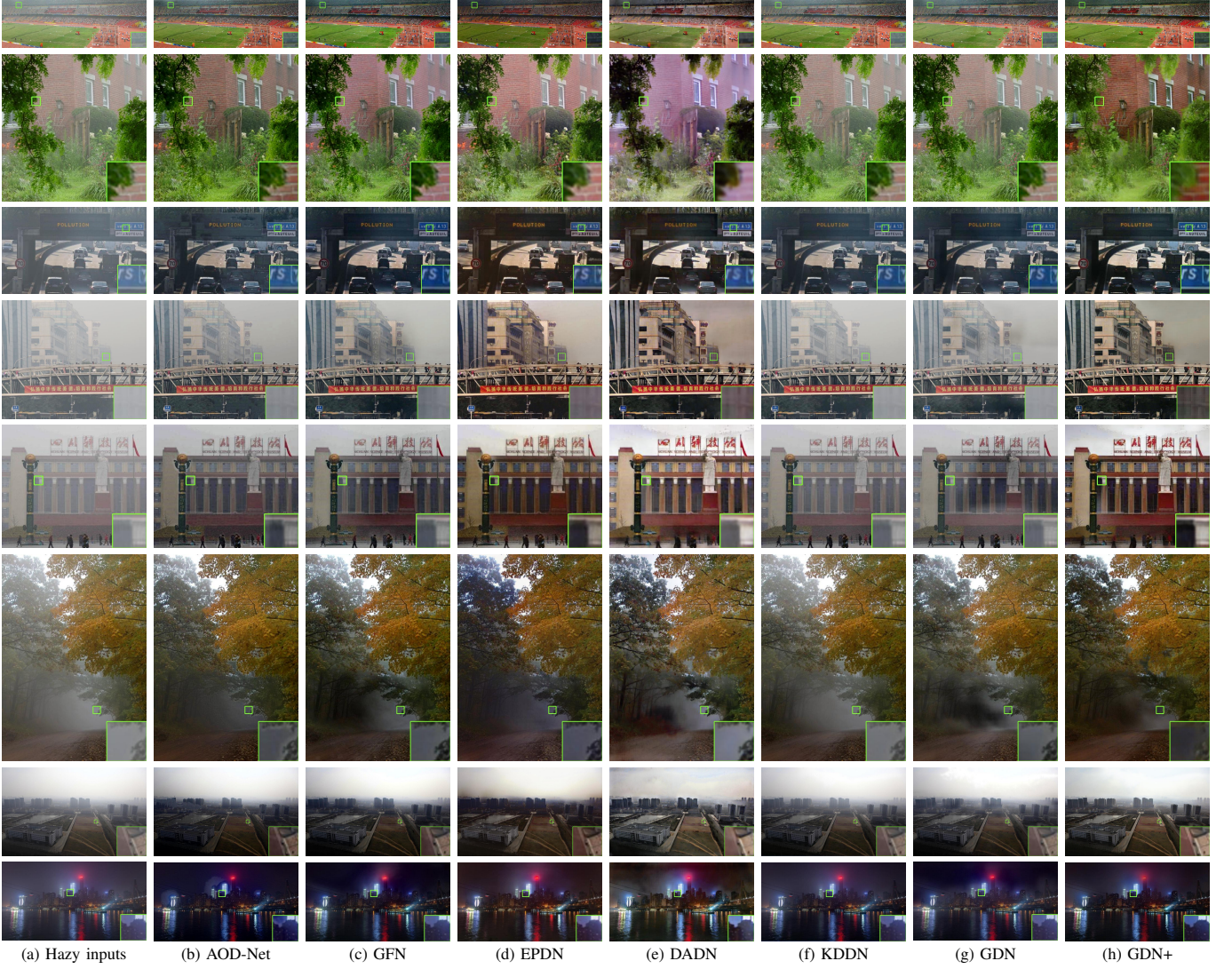


Fig. 9. Visual comparisons of different methods on real hazy images: the ones in the first 2 rows are from 37Real, and the rest are from URHI. Zoom in for details.

Ratio (PSNR) and Structure Similarity Index Measure (SSIM) to evaluate the dehazing results of different methods. Note that the official codes of some compared methods are not publicly available. For fair comparisons, we laboriously implement them by ourselves and make sure that they can reproduce the results reported in their original papers.

B. Evaluations on Synthetic Data

We conduct both quantitative and qualitative evaluations on the 4 synthetic benchmarks, namely, SOTS, Middlebury, HazeRD, and O-HAZE. Comparisons in terms of average PSNR/SSIM values can be found in Tab I. It is evident that the proposed GDN+ outperforms the KDDN and DADN by a large margin, and shows a noticeable improvement over its preliminary version GDN (*e.g.*, 0.64 dB on SOTS). Visual comparisons on the tested benchmarks can be found in Fig. 8. Note that the AOD-Net suffers from the halo artifacts in some cases (*e.g.*, the 5th row of Fig. 8 (b)). The GFN and EPDN can largely overcome this problem, but while dealing with dense haze, their dehazing performance is limited (*e.g.*, the 7th row

of Figs. 8 (c-d)). The DADN tends to cause color distortions (*e.g.*, the 4th and 5th rows in Fig. 8 (e)). As for the KDDN, the output still remains a non-negligible amount of haze in some cases (*e.g.*, the 1st row of Fig. 8 (f)).

Compared to these methods, the proposed GDN+ has the best performance in terms of haze removal and artifact/distortion suppression. Our dehazing results are free of major artifacts/distortions and are visually most similar to the ground-truth.

C. Evaluation on Real Data

We further compare the GDN+ with the SOTA methods on 2 real datasets, namely, 37Real and URHI. Here we shall only make qualitative evaluations since the haze-free counterparts of the real hazy images in these two datasets are not available. As shown in Fig. 9, the dehazing results on real data are quite consistent with those on synthetic data. The AOD-Net again suffers from the halo artifacts (*e.g.*, the 6th rows of Fig. 9 (b)). The GFN and EPDN have difficulty in dealing with dense haze (*e.g.*, the 6th rows of Figs. 9 (c-d)). The DADN may

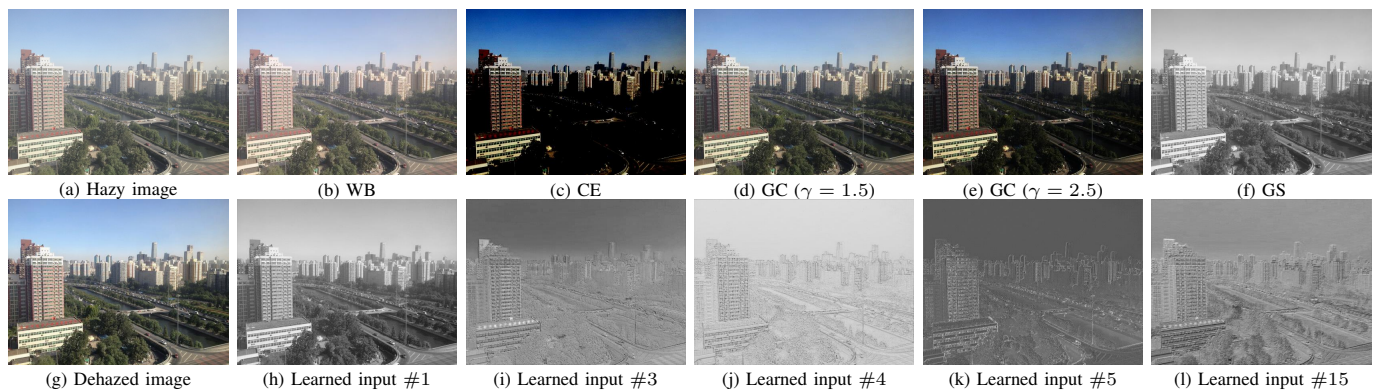


Fig. 10. Visualization of the derived and learned inputs for a hazy image from SOTS.

cause severe color distortions (*e.g.*, the 2th row of Fig. 9 (e)). Due to domain shift, the KDDN fails to achieve the favorable dehazing results in real-world scenarios (*e.g.*, the 2nd and 4th rows of Fig. 9 (f)).

Compared to these methods, the proposed GDN+ removes haze more thoroughly and is free of color distortion. The GDN+ also delivers better dehazing results on real data than its preliminary version GDN. This improvement can be attributed to the proposed ITKT mechanism that uses translated data to alleviate domain shift and assists the learning process on such data with the knowledge distilled from the corresponding synthetic data.

D. Necessity of the Atmosphere Scattering Model

To gain a better understanding of the difference between the direct estimation strategy where the ASM is completely bypassed (denoted as *Direct*) and the indirect estimation strategy where the transmission map and the atmospheric light intensity are first estimated and then leveraged to calculate the dehazing result (denoted as *Indirect*), we adjust the GDN+ to make it follow the indirect estimation strategy instead. Specifically, we modify the convolution at the output end (*i.e.*, the rightmost Conv@K3S1 in Fig. 3) so that it outputs two feature maps rather than three. The first feature map is used as the estimated transmission map while the mean of the second one serves as the estimated atmospheric light intensity. These two estimates are then substituted into Eq. (1) to calculate the dehazing result. This variant of the GDN+ is trained in the same way as detailed in Sec. V-A. It is then quantitatively evaluated on the SOTS and HazeRD, and compared with its original version. Note that both the SOTS and HazeRD are synthetic datasets based the ASM. So as far as this kind of testing datasets are concerned, the indirect estimation strategy essentially takes advantage of the ASM as a perfect prior.

However, as shown in Tab. II, although adopting the ASM leads to a significant reduction in the number of parameters to be estimated, it in fact incurs performance degradation. This indicates that incorporating the ASM into the GDN+ does have a detrimental effect on the loss surface.

E. Utility of Learned Inputs

The pre-processing module of the GDN+ produces 16 learned inputs in total. Here we build two variants of the GDN+ to demonstrate the diversity gain offered by these learned inputs. For the first variant (denoted as *Original*), we remove the pre-processing module and replace the first 3 learned inputs by the RGB channels of the given RGB hazy image and the rest by all-zero feature maps. For the second variant (denoted as *Derived*), the learned inputs are substituted with the same number of derived inputs generated by hand-selected pre-processing methods. More specifically, we generate 16 derived inputs, 3 from the given hazy image, 3 from the White Balanced (WB) image, 3 from the Contrast Enhanced (CE) image, 6 from two Gamma Corrected (GC) images with γ set to 1.5 and 2.5 respectively, and 1 from the Gray-Scaled (GS) image. Fig. 10 shows the derived and learned inputs of a hazy image.

Although the hand-selected pre-processing methods can create diversified inputs, our pre-processing module is considerably more flexible and adaptive in finetuning the given image to better suit the follow-up process (*e.g.*, the learned inputs #3 and #5 enhance different aspects of the given hazy image and are complement to each other). More interestingly, the learned input #1 resembles a GS image, even though this is not prescribed. This shows that our pre-processing module is capable of mimicking hand-selected pre-processing methods when it is beneficial to do so.

TABLE II
QUANTITATIVE COMPARISONS OF DIFFERENT ESTIMATION STRATEGIES.
THE BEST ONE IS HIGHLIGHTED IN **BOLD**.

Method	Indirect	Direct (GDN+)
SOTS	31.82/0.9732	32.15/0.9777
HazeRD	17.81/0.8455	19.54/0.8697

TABLE III
QUANTITATIVE COMPARISONS OF DIFFERENT INPUT TYPES. THE BEST
ONE IS HIGHLIGHTED IN **BOLD**.

Method	Original	Derived	Learned (GDN+)
SOTS	30.04/0.9697	29.08/0.9635	32.15/0.9777
HazeRD	17.69/0.8486	18.04/0.8580	19.54/0.8697

TABLE IV
QUANTITATIVE COMPARISONS OF DIFFERENT VARIANTS OF GDN+. THE BEST ONE IS HIGHLIGHTED IN **BOLD**.

Method	EDNet	MSNet	w/o SCAB	w/o CAB	w/o SAB	w/o post-processing	Our GDN+
SOTS	25.98/0.9446	27.65/0.9467	27.85/0.9657	29.31/0.9734	31.80/0.9759	31.79/0.9755	32.15/0.9777
HazeRD	15.86/0.8182	16.51/0.8208	15.91/0.8264	16.12/0.8295	19.05/0.8648	19.28/0.8669	19.54/0.8697

To further validate the effectiveness of learned inputs, we follow the same experimental setup to train both variants, and quantitatively evaluate their dehazing performance on the SOTS and HazeRD. Tab. III shows that the GDN+ with learned inputs (denoted as *Learned*) outperforms the *Original* and *Derived* versions in terms of PSNR and SSIM values.

F. Validation of the Overall Design

The proposed GDN+ is a multi-scale network that is enhanced in two aspects: 1) a grid structure with dense connections across different scales to facilitate the information exchange, and 2) novel SCABs that are capable of fusing features based on their relative importance to dehazing. To demonstrate the effectiveness of the adopted grid structure, we consider the following two variants: 1) the Encoder-Decoder Network (*EDNet*) obtained by pruning the GDN+ (see the red path in Fig. 3), and 2) the conventional multi-scale network (*MSNet*) resulted from removing all exchange branches except for the first and the last ones to maintain the minimum connection. To validate the proposed SCAB, we consider the following three variants: 1) the GDN+ without SCABs (*w/o SCAB*), 2) the GDN+ with CAB-absent SCABs (*w/o CAB*), and 3) the GDN+ with SAB-absent SCABs (*w/o SAB*). In addition, we build a variant of the GDN+ that has no post-processing module (*w/o post-processing*). All these variants are trained in the same way as before and are tested on the SOTS and HazeRD.

The quantitative comparisons are shown in Table IV. Compared to the *EDNet* and *MSNet*, the proposed GDN+ achieves favorable dehazing results owing to the superiority of the grid structure. Besides, it can be seen that the variants *w/o SAB* and *w/o CAB* both outperform the baseline *w/o SCAB* though the performance gain from CAB appears to be more significant than that from SAB. Benefiting from the contributions of both CAB and SAB, the GDN+ with SCABs delivers further elevated performance. As compared to the GDN+, the dehazing performance of *w/o post-processing* is inferior owing to the potential residual artifacts in the outputs from the backbone module. The above results provide a rather comprehensive justification of the overall design of the proposed GDN+.

G. Effectiveness of the Intra-Task Knowledge Transfer Mechanism

To convincingly demonstrate the effectiveness of the proposed ITKT mechanism, we build a variant (*w/o ITKT*) by removing the entire teacher network and training the student network directly on translated data. We adopt the exactly same experimental setup to train this variant. Real datasets usually do not contain the the ground-truth, rendering quantitative

TABLE V
QUANTITATIVE COMPARISONS OF ITKT-RELATED VARIANTS ON SOTS-T. THE BEST ONE IS HIGHLIGHTED IN **BOLD**.

Method	Teacher	w/o ITKT	w/ ITKT (GDN+)
SOTS-T	21.08/0.8004	23.70/0.8606	24.66/0.8751

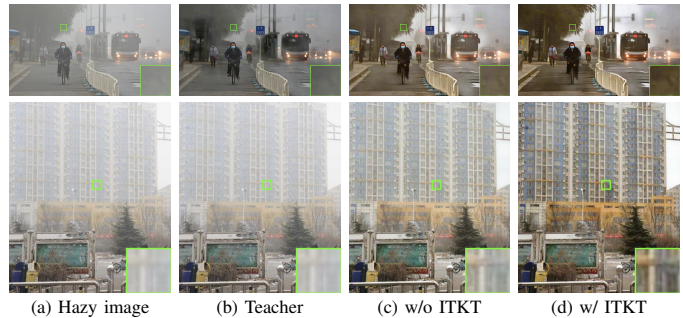


Fig. 11. Qualitative comparisons of ITKT-related variants on real hazy images from URHI.

evaluations infeasible. To address this issue, we generate a translated version of the original SOTS, named SOTS-T, and leverage it for quantitative comparisons. Besides *w/o ITKT* and *w/ ITKT* (i.e., *GDN+*), the teacher network (*Teacher*) trained on synthetic data is also tested on the SOTS-T.

According to Tab. V, the knowledge distilled from synthetic data does benefit the learning process on translated data. Indeed, *w/ ITKT* achieves higher PSNR and SSIM values on the SOTS-T as compared to *w/o ITKT*. It can be seen from Figs. 11 (c-d) that *w/ ITKT* removes haze more thoroughly than *w/o ITKT*, and produces more appealing dehazing results. Also note that *Teacher* achieves 32.15 dB in PSNR on synthetic data but only 21.08 dB on translated data, and performs poorly on real hazy images as shown in Fig. 11 (b). This dramatic performance drop is owing to the domain discrepancy between training and testing data. Therefore, it is necessary to conduct training on real data or those with (approximately) the same distribution. This is exactly the rationale underlying our introduction of translated data and the teacher-student structure with ITKT. It is worth emphasizing that the proposed ITKT mechanism is generic in nature and can be easily employed in other learning-based dehazing methods to improve their performance on real hazy images.

H. Runtime Analysis

Here we compare the model complexity and computational efficiency of the proposed GDN+ against other dehazing methods. Tab. VI shows the model size of each method in terms of the number of parameters in thousand (in K) and their

TABLE VI
THE MODEL SIZE AND RUNTIME (IN S) OF DIFFERENT DEHAZING METHODS. THE BEST ONE IS HIGHLIGHTED IN **BOLD**.

Method	DCP	DehazeNet	AOD-Net	GFN	EPDN	DADN	KDDN	GDN	GDN+
# Params. (K)	-	7.8	1.8	212.1	17,379.2	54,591.4	2,404.9	958.1	961.0
Runtime (s)	166.18	3.70	0.46	0.84	0.32	1.13	0.28	0.40	2.19



Fig. 12. Failure case. Our GDN+ might perform poorly when dealing with varicolored haze.

runtime in second (in s) on a 1,080P fake dataset, where all pixel values are set to 1. Note that except for the DCP that only works on CPU, all the others can be run on GPU. The proposed GDN+ has fewer parameters than recently developed dehazing methods such as KDDN and DADN, and our un-optimized code takes about 2.19s to process one 1,080P image. The comparison between the GDN+ and its preliminary version GDN reveals that the adoption of self-attentions has a very mild impact on the model size, but comes at the cost of runtime.

I. Failure Case

In reality, the color of haze is not always purely white due to chromatic casts caused by colored lights or pollution. Since the issue of varicolored haze is not specifically addressed during the training process, the dehazing result by GDN+ might be contaminated by the haze color. For instance, as shown in Fig. 12, even though the GDN+ successfully removes most of the haze effect, the result still appears pinkish. Recently, reference [62] tackles this color distortion problem by introducing a color correction module to whiten varicolored haze before the dehazing process. It is expected that the same approach can be used to improve the ability of our method in dealing with the situation encountered in Fig. 12.

VI. CONCLUSION

We have proposed an enhanced multi-scale network and demonstrated its competitive performance for single image dehazing. The design of this network involves several ideas. We adopt a densely connected grid structure to facilitate the information exchange across different scales. Novel SCABs, constructed based on the idea of self-attentions, are placed at the junctions of the grid structure to enable adaptive feature fusion. The issue of domain shift is addressed by converting synthetic data to translated data with the distribution matched to that of real hazy images. We further propose a new ITKT mechanism that leverages the knowledge distilled from

synthetic data to assist the learning process on translated data, and realize this mechanism through a teacher-student structure.

Due to the generic nature of its building components, the proposed network is expected to be applicable to a wide range of image restoration problems. Investigating such applications is an endeavor well worth undertaking.

Our work also sheds some light on the puzzling phenomenon regarding the use of the ASM in image dehazing, and suggests the need to rethink the role of physical models in the design of image restoration algorithms.

REFERENCES

- [1] E. J. McCartney, "Optics of the atmosphere: scattering by molecules and particles," *New York, John Wiley and Sons, Inc.*, 1976. 421 p., 1976.
- [2] S. G. Narasimhan and S. K. Nayar, "Chromatic framework for vision in bad weather," in *IEEE Conference on Computer Vision and Pattern Recognition (CVPR)*, vol. 1, 2000, pp. 598–605.
- [3] —, "Vision and the atmosphere," *International Journal of Computer Vision (IJCV)*, vol. 48, no. 3, pp. 233–254, 2002.
- [4] X. Liu, Y. Ma, Z. Shi, and J. Chen, "Griddehazenet: Attention-based multi-scale network for image dehazing," in *Proceedings of the IEEE/CVF International Conference on Computer Vision*, 2019, pp. 7314–7323.
- [5] Y. Shao, L. Li, W. Ren, C. Gao, and N. Sang, "Domain adaptation for image dehazing," in *Proceedings of the IEEE/CVF Conference on Computer Vision and Pattern Recognition*, 2020, pp. 2808–2817.
- [6] B. Li, W. Ren, D. Fu, D. Tao, D. Feng, W. Zeng, and Z. Wang, "Benchmarking single-image dehazing and beyond," *IEEE Transactions on Image Processing (TIP)*, vol. 28, no. 1, pp. 492–505, 2019.
- [7] T. Tong, G. Li, X. Liu, and Q. Gao, "Image super-resolution using dense skip connections," in *IEEE International Conference on Computer Vision (ICCV)*, 2017, pp. 4799–4807.
- [8] W. Ren, L. Ma, J. Zhang, J. Pan, X. Cao, W. Liu, and M.-H. Yang, "Gated fusion network for single image dehazing," in *IEEE Conference on Computer Vision and Pattern Recognition (CVPR)*, 2018, pp. 3253–3261.
- [9] Z. Shen, W.-S. Lai, T. Xu, J. Kautz, and M.-H. Yang, "Deep semantic face deblurring," in *IEEE Conference on Computer Vision and Pattern Recognition (CVPR)*, 2018, pp. 8260–8269.
- [10] C. Chen, Q. Chen, J. Xu, and V. Koltun, "Learning to see in the dark," in *IEEE Conference on Computer Vision and Pattern Recognition (CVPR)*, 2018, pp. 3291–3300.
- [11] J.-Y. Zhu, T. Park, P. Isola, and A. A. Efros, "Unpaired image-to-image translation using cycle-consistent adversarial networks," in *Proceedings of the IEEE international conference on computer vision*, 2017, pp. 2223–2232.
- [12] Y. Y. Schechner, S. G. Narasimhan, and S. K. Nayar, "Instant dehazing of images using polarization," in *IEEE Conference on Computer Vision and Pattern Recognition (CVPR)*, 2001, pp. 325–332.
- [13] S. Shwartz, E. Namer, and Y. Y. Schechner, "Blind haze separation," in *IEEE Conference on Computer Vision and Pattern Recognition (CVPR)*, vol. 2, 2006, pp. 1984–1991.
- [14] S. G. Narasimhan and S. K. Nayar, "Contrast restoration of weather degraded images," *IEEE Transactions on Pattern Analysis and Machine Intelligence (TPAMI)*, no. 6, pp. 713–724, 2003.
- [15] S. K. Nayar and S. G. Narasimhan, "Vision in bad weather," in *IEEE International Conference on Computer Vision (ICCV)*, vol. 2, 1999, pp. 820–827.
- [16] S. G. Narasimhan and S. K. Nayar, "Interactive (de) weathering of an image using physical models," in *IEEE Workshop on Color and Photometric Methods in Computer Vision*, vol. 6. France, 2003.

- [17] J. Kopf, B. Neubert, B. Chen, M. Cohen, D. Cohen-Or, O. Deussen, M. Uyttendaele, and D. Lischinski, *Deep photo: Model-based photograph enhancement and viewing*. ACM, 2008, vol. 27.
- [18] R. T. Tan, "Visibility in bad weather from a single image," in *IEEE Conference on Computer Vision and Pattern Recognition (CVPR)*, 2008, pp. 1–8.
- [19] R. Fattal, "Single image dehazing," *ACM Transactions on Graphics (TOG)*, vol. 27, no. 3, p. 72, 2008.
- [20] K. He, J. Sun, and X. Tang, "Single image haze removal using dark channel prior," *IEEE Transactions on Pattern Analysis and Machine Intelligence (TPAMI)*, vol. 33, no. 12, pp. 2341–2353, 2011.
- [21] K. Tang, J. Yang, and J. Wang, "Investigating haze-relevant features in a learning framework for image dehazing," in *IEEE Conference on Computer Vision and Pattern Recognition (CVPR)*, 2014, pp. 2995–3000.
- [22] Q. Zhu, J. Mai, and L. Shao, "A fast single image haze removal algorithm using color attenuation prior," *IEEE Transactions on Image Processing (TIP)*, vol. 24, no. 11, pp. 3522–3533, 2015.
- [23] W. Ren, S. Liu, H. Zhang, J. Pan, X. Cao, and M.-H. Yang, "Single image dehazing via multi-scale convolutional neural networks," in *European conference on computer vision (ECCV)*. Springer, 2016, pp. 154–169.
- [24] B. Cai, X. Xu, K. Jia, C. Qing, and D. Tao, "Dehazenet: An end-to-end system for single image haze removal," *IEEE Transactions on Image Processing (TIP)*, vol. 25, no. 11, pp. 5187–5198, 2016.
- [25] H. Zhang and V. M. Patel, "Densely connected pyramid dehazing network," in *Proceedings of the IEEE conference on computer vision and pattern recognition*, 2018, pp. 3194–3203.
- [26] J. Dong and J. Pan, "Physics-based feature dehazing networks," in *European Conference on Computer Vision*. Springer, 2020, pp. 188–204.
- [27] B. Li, X. Peng, Z. Wang, J. Xu, and D. Feng, "Aod-net: All-in-one dehazing network," in *IEEE International Conference on Computer Vision (ICCV)*, 2017, pp. 4770–4778.
- [28] Y. Qu, Y. Chen, J. Huang, and Y. Xie, "Enhanced pix2pix dehazing network," in *Proceedings of the IEEE/CVF Conference on Computer Vision and Pattern Recognition*, 2019, pp. 8160–8168.
- [29] L. Li, Y. Dong, W. Ren, J. Pan, C. Gao, N. Sang, and M.-H. Yang, "Semi-supervised image dehazing," *IEEE Transactions on Image Processing*, vol. 29, pp. 2766–2779, 2019.
- [30] G. Hinton, O. Vinyals, and J. Dean, "Distilling the knowledge in a neural network," *arXiv preprint arXiv:1503.02531*, 2015.
- [31] A. Romero, N. Ballas, S. E. Kahou, A. Chassang, C. Gatta, and Y. Bengio, "Fitnets: Hints for thin deep nets," *arXiv preprint arXiv:1412.6550*, 2014.
- [32] T. Wang, L. Yuan, X. Zhang, and J. Feng, "Distilling object detectors with fine-grained feature imitation," in *Proceedings of the IEEE/CVF Conference on Computer Vision and Pattern Recognition*, 2019, pp. 4933–4942.
- [33] Y. Wang, W. Zhou, T. Jiang, X. Bai, and Y. Xu, "Intra-class feature variation distillation for semantic segmentation," in *European Conference on Computer Vision*. Springer, 2020, pp. 346–362.
- [34] H. Yin, P. Molchanov, J. M. Alvarez, Z. Li, A. Mallya, D. Hoiem, N. K. Jha, and J. Kautz, "Dreaming to distill: Data-free knowledge transfer via deepinversion," in *Proceedings of the IEEE/CVF Conference on Computer Vision and Pattern Recognition*, 2020, pp. 8715–8724.
- [35] X. Chen, Y. Zhang, Y. Wang, H. Shu, C. Xu, and C. Xu, "Optical flow distillation: Towards efficient and stable video style transfer," in *European Conference on Computer Vision*. Springer, 2020, pp. 614–630.
- [36] H. Wu, J. Liu, Y. Xie, Y. Qu, and L. Ma, "Knowledge transfer dehazing network for nonhomogeneous dehazing," in *Proceedings of the IEEE/CVF Conference on Computer Vision and Pattern Recognition Workshops*, 2020, pp. 478–479.
- [37] M. Hong, Y. Xie, C. Li, and Y. Qu, "Distilling image dehazing with heterogeneous task imitation," in *Proceedings of the IEEE/CVF Conference on Computer Vision and Pattern Recognition*, 2020, pp. 3462–3471.
- [38] A. Choromanska, M. Henaff, M. Mathieu, G. B. Arous, and Y. LeCun, "The loss surfaces of multilayer networks," in *Artificial Intelligence and Statistics*, 2015, pp. 192–204.
- [39] F. Draxler, K. Veschgini, M. Salmhofer, and F. A. Hamprecht, "Essentially no barriers in neural network energy landscape," *arXiv preprint arXiv:1803.00885*, 2018.
- [40] Q. Nguyen and M. Hein, "The loss surface and expressivity of deep convolutional neural networks," 2018.
- [41] D. Fourure, R. Emonet, E. Fromont, D. Muselet, A. Tremeau, and C. Wolf, "Residual conv-deconv grid network for semantic segmentation," *arXiv preprint arXiv:1707.07958*, 2017.
- [42] B. Mildenhall, J. T. Barron, J. Chen, D. Sharlet, R. Ng, and R. Carroll, "Burst denoising with kernel prediction networks," in *IEEE Conference on Computer Vision and Pattern Recognition (CVPR)*, 2018, pp. 2502–2510.
- [43] Y. Zhang, Y. Tian, Y. Kong, B. Zhong, and Y. Fu, "Residual dense network for image super-resolution," in *IEEE Conference on Computer Vision and Pattern Recognition (CVPR)*, 2018, pp. 2472–2481.
- [44] X. Tao, H. Gao, X. Shen, J. Wang, and J. Jia, "Scale-recurrent network for deep image deblurring," in *IEEE Conference on Computer Vision and Pattern Recognition (CVPR)*, 2018, pp. 8174–8182.
- [45] X. Wang, R. Girshick, A. Gupta, and K. He, "Non-local neural networks," in *Proceedings of the IEEE conference on computer vision and pattern recognition*, 2018, pp. 7794–7803.
- [46] S. Woo, J. Park, J.-Y. Lee, and I. S. Kweon, "Cbam: Convolutional block attention module," in *Proceedings of the European conference on computer vision (ECCV)*, 2018, pp. 3–19.
- [47] R. Girshick, "Fast r-cnn," in *IEEE International Conference on Computer Vision (ICCV)*, 2015, pp. 1440–1448.
- [48] J. Johnson, A. Alahi, and L. Fei-Fei, "Perceptual losses for real-time style transfer and super-resolution," in *European Conference on Computer Vision (ECCV)*. Springer, 2016, pp. 694–711.
- [49] K. Simonyan and A. Zisserman, "Very deep convolutional networks for large-scale image recognition," *arXiv preprint arXiv:1409.1556*, 2014.
- [50] O. Russakovsky, J. Deng, H. Su, J. Krause, S. Satheesh, S. Ma, Z. Huang, A. Karpathy, A. Khosla, M. Bernstein et al., "Imagenet large scale visual recognition challenge," *International Journal of Computer Vision (IJCV)*, vol. 115, no. 3, pp. 211–252, 2015.
- [51] N. Silberman, D. Hoiem, P. Kohli, and R. Fergus, "Indoor segmentation and support inference from rgb-d images," in *European Conference on Computer Vision (ECCV)*. Springer, 2012, pp. 746–760.
- [52] D. Scharstein and R. Szeliski, "High-accuracy stereo depth maps using structured light," in *IEEE Conference on Computer Vision and Pattern Recognition (CVPR)*, vol. 1, 2003.
- [53] F. Liu, C. Shen, G. Lin, and I. Reid, "Learning depth from single monocular images using deep convolutional neural fields," *IEEE Transactions on Pattern Analysis and Machine Intelligence (TPAMI)*, vol. 38, no. 10, pp. 2024–2039, 2016.
- [54] C. Ancuti, C. O. Ancuti, and C. De Vleeschouwer, "D-hazy: A dataset to evaluate quantitatively dehazing algorithms," in *2016 IEEE International Conference on Image Processing (ICIP)*. IEEE, 2016, pp. 2226–2230.
- [55] Y. Zhang, L. Ding, and G. Sharma, "Hazerd: an outdoor scene dataset and benchmark for single image dehazing," in *2017 IEEE international conference on image processing (ICIP)*. IEEE, 2017, pp. 3205–3209.
- [56] C. O. Ancuti, C. Ancuti, R. Timofte, and C. De Vleeschouwer, "O-haze: a dehazing benchmark with real hazy and haze-free outdoor images," in *Proceedings of the IEEE conference on computer vision and pattern recognition workshops*, 2018, pp. 754–762.
- [57] C. Ancuti, C. O. Ancuti, and R. Timofte, "Ntire 2018 challenge on image dehazing: Methods and results," in *Proceedings of the IEEE Conference on Computer Vision and Pattern Recognition Workshops*, 2018, pp. 891–901.
- [58] R. Fattal, "Dehazing using color-lines," *ACM Transactions on Graphics (TOG)*, vol. 34, no. 1, p. 13, 2014.
- [59] D. P. Kingma and J. Ba, "Adam: A method for stochastic optimization," *arXiv preprint arXiv:1412.6980*, 2014.
- [60] S. Nah, T. Hyun Kim, and K. Mu Lee, "Deep multi-scale convolutional neural network for dynamic scene deblurring," in *IEEE Conference on Computer Vision and Pattern Recognition (CVPR)*, 2017, pp. 3883–3891.
- [61] B. Lim, S. Son, H. Kim, S. Nah, and K. Mu Lee, "Enhanced deep residual networks for single image super-resolution," in *IEEE Conference on Computer Vision and Pattern Recognition Workshops (CVPRW)*, 2017, pp. 136–144.
- [62] A. Dudhane, K. M. Biradar, P. W. Patil, P. Hambarde, and S. Murala, "Varicolored image de-hazing," in *Proceedings of the IEEE/CVF Conference on Computer Vision and Pattern Recognition*, 2020, pp. 4564–4573.